Research Article

Investigating the thermal stability of nanocrystalline aluminum-lithium alloy by combining different mechanisms: Reinforcing with graphene and alloying with Sr

Sara I. Ahmad[a], Hicham Hamoudi[b], Atef Zekri[b], Khaled M. Youssef[a],*

[a] *Materials Science and Technology Graduate Program, College of Arts and Sciences, Qatar University, Doha 2713, Qatar*
[b] *Qatar Environment and Energy Research Institute, Doha 34110, Qatar*

ARTICLE INFO

ABSTRACT

Interest in nanocrystalline (nc) aluminum-lithium (Al-Li) alloys is motivated by the demand for lightweight and high-performance materials for light-weighting applications and superior fuel consumption. Nonetheless, nc metals, including Al are thermally unstable, which hinders their technological applications. In this study, we explore the effect of combining dilute amounts of strontium (1.0 at% Sr) and graphene nanoplatelets (1.0 wt% GNPs) to investigate the thermal stability of a nc Al-Li alloy. Ball milling was used to prepare four samples: Al-Li, Al-Li-Sr, Al-Li-GNPs, and Al-Li-Sr-GNPs, to systematically investigate the role of each added element. Isothermal annealing was conducted at different temperatures to investigate the thermal stability. Despite maintaining a nanometric grain size and high hardness of 70 nm and 1.1 GPa, respectively, after annealing at 773 K for 1 h, the Al-Li-Sr-GNPs sample suffered the most significant grain growth and the highest drop in hardness when compared to the Al-Li-Sr and Al-Li-GNPs samples. Microstructural investigations suggested that competing effects resulting from the spontaneous reaction of both Sr and GNPs with Al at higher temperatures resulted in a declining thermal stability efficiency. The formation and distribution of the rod-like Al_4C_3 phase at the grain boundaries stood in the way of proper Sr diffusion after annealing and caused the agglomeration of the Al_4Sr phase.

1. Introduction

It is well-known that reducing the grain size of metals from the conventional microscale to the nanoscale (< 100 nm) [1] can cause significant enhancements in their mechanical strength and hardness [2–4]. The yield strength dependence on grain size is generally expressed as the Hall-Petch relationship [5]. However, nanocrystalline metals are inherently unstable at elevated temperatures because the nanoscale grain size provides an enormous driving force for grain growth which hinders their technological applications [1].

Nonetheless, optimistic studies demonstrated that thermal stability in nanocrystalline metals is possible up to high homologous temperatures but only in multicomponent systems [1,6]. That is, the thermal stability induced to the nanocrystalline matrix stemmed from the incorporation of impurities, solutes, second phases, and/or reinforcements through their interactions with the main nanocrystalline metal. According to the nature of these interactions, thermal

stability can be achieved in two different mechanisms [7]. First, a kinetic approach where these elements, either solutes or second phases, act as pinning points providing a dragging force to restrict the mobility of the grain boundaries of the main matrix [6]. Otherwise, a thermodynamic approach is possible where the secondary elements, usually a solute that has a large value of elastic enthalpy and is insoluble within the solvent matrix, segregate to the grain boundaries to release the excess stresses associated with their presence in the grains, reducing the grain boundary energy and eliminating the driving force for grain growth [6].

Several studies have investigated the thermal stability of nanocrystalline Al and Al alloys [8–10]. A modified Wynblatt-Ku thermodynamic model [11,12] predicted the efficiency of doping Al with dilute amounts of Sr (1.0 at%) to achieve both kinetic and thermodynamic stabilities at high temperatures. The justification for the selection of Sr as a dopant to thermally stabilize Al is its limited solubility in Al, the large lattice misfit between the Al and Sr atoms, and the large negative enthalpy of mixing of Sr in Al, all of which favor Sr segregation into the Al grain boundaries [6]. Such behavior is the basis for achieving thermodynamic stability. Experimentally,

---

* Corresponding author.
E-mail address: kyoussef@qu.edu.qa (K.M. Youssef).

ball-milled nanocrystalline Al proved to be thermally stable up to 873 K (which represents 90% of Al's melting point) by the addition of 1.0 at% Sr [11].

Recently, attention to enhancing the mechanical performance of Al has shifted from synthesizing nanocrystalline Al to reinforcing Al-based matrices with nano reinforcements such graphene nanoplatelets (GNPs) [13]. The two-dimensional nanoparticles have been established as an efficient reinforcement for the synthesis of high-performance Al matrix composites with reported enhancements in both the strength and hardness of Al [14–17]. Interestingly, studies reporting the mechanical performance of GNPs reinforced Al have also reported that the GNPs played an important role in preventing grain growth at high temperatures. Thus, in addition to the enhancement in the mechanical performance, the introduction of GNPs into nano-sized Al matrices is suggested as a significant strategy for establishing thermal stability [18–21]. Khorshid et al. [18] reported an insignificant grain growth from 68.5 nm to 85.9 nm after annealing the ball-milled and hot-pressed Al-0.5 wt% GNPs nanocomposite at 535° C for 24 h. It was suggested in these studies that the grain growth was eliminated by the presence of GNPs or Al_4C_3 second phase, which pins the grain boundary motion during high-temperature processes.

Conventional Al-Li alloys are well-known for their high specific strength, which renders them reliable for structural, aerospace, transportation, and military applications. In addition, recent studies reported successful nano-structuring and synthesis of nanocrystalline Al-Li alloys with high strength and good ductility [22,23]. Nonetheless, their thermal stability behavior has not been investigated yet to the best of our knowledge. Achieving thermal stability requires the careful design of the system's constituents to orchestrate the best possible thermal stability mechanism. Furthermore, exploring different strategies of thermal stability is significantly essential to establish a scientific understanding that allows for different approaches to be put for minimizing grain growth.

In this regard, we explore the effect of combining dilute amounts of two different elements, GNPs and Sr, which have proven to individually exert a positive impact on the thermal stability of nanocrystalline Al-Li alloys, to achieve an enhanced thermal stability behavior of nanocrystalline Al. Remarkably, experimental investigations showed that instead of an enhanced two-elements induced thermal stability behavior, competing effects resulting from the spontaneous reaction of both Sr and graphene with Al at higher temperatures resulted in a reduced thermal stability efficiency.

2. Materials and methods

2.1. Materials and synthesis

The starting Al-alloy comprised of pure Al powders (99.97% purity and an average particle size of 15 μm, Alfa Aesar, CAS# 7439-90-5) and Li granules (99% purity and a granule size ranging between 3 and 6 mm, Sigma-Aldrich, CAS# 7439-93-2). The thermal stability elements consisted of GNPs (Sigma-Aldrich, CAS# 799084) and Sr pieces (99.8% purity, Alfa Aesar, CAS# 7440–24–6). In order to compare the effect of both Sr and GNPs individually before combining both elements, four different samples were investigated: Al-2.0 at% Li, Al-2.0 at% Li −1.0 at% Sr, Al-2.0 at% Li −1.0 wt% GNPs, and Al-2.0 at% Li −1.0 at% Sr–1.0 wt% GNPs. Only 2.0 at% Li were added to Al to synthesize an Al-2.0 at% Li alloy which ensures the solid solubility of Li in Al [24,25]. A dilute amount of 1.0 at% Sr was selected to produce a non-equilibrium solid solution in the Al alloy and induce thermodynamic stability [11]. The 1.0 wt% GNPs content was based on literature data which reported an optimum Al/GNPs behavior with the addition of 1.0 wt% GNPs in Al composites [16,26].

The ball-milling process was used to synthesize the samples mentioned above. The milling process was set to serve several purposes: to achieve grain refinement of the Al-based matrix, alloy Al with Li and Sr, and distribute the GNPs homogenously within the alloy. The GNPs containing samples (Al-Li-GNPs and Al-Li-Sr-GNPs) were milled using a high-energy SPEX8000 shaker-mill for 8 h. While in the absence of GNPs, the Al-Li and Al-Li-Sr sample were cryomilled for 4 h using the Retsch Cryomill. It is common practice to use a process control agent (PCA) or a surfactant during the milling of ductile metals such as Al to eliminate excessive welding and encourage nano-structuring. However, such organic materials can present unwanted impurities in the milled powder and are not utilized in this study. Instead, the welding of the highly ductile Al powder was mitigated by the presence of the GNPs in the GNPs containing samples (Al-Li-GNPs and Al-Li-Sr-GNPs). The self-lubricating nature of GNPs stems from the weak van der Waals attraction forces between the graphene sheets, which causes the sheets to slide easily with respect to one another [27], thus acting as a PCA during milling. As a result, room temperature milling was successful, and the final sample consisted of fine powders when room temperature milling was conducted for the GNPs containing samples.

On the contrary, excessive welding occurred during the room temperature milling of the Al-Li-Sr sample. Therefore, the Al-Li and Al-Li-Sr samples were synthesized using cryomilling, which operated at liquid N_2 temperatures to overcome the heat generated during milling and embrittle the ductile Al to promote its fracture. Prior to milling, the starting material and the stainless-steel milling balls (ball-to-powder ratio of 17:1) were loaded in a stainless-steel milling vial in a MBRAUN LABstar glovebox operating under an ultra-high pure argon atmosphere ($O_2 < 0.5$ ppm). No process control agents were used in the milling process.

2.2. Thermal stability investigations

To investigate the degree of thermal stability of the as-milled samples, isothermal annealing was conducted in a GSL-1500X-RTP50 tube furnace at 773 K and 873 K for 1 h. The annealing was conducted at a rate of 10°/min under a protective atmosphere of a mixed gas (98% Ar + 2% H_2) to avoid oxidation. The furnace tube was evacuated (~2 × 10^{-5} bar) and refilled with the mixed gas at least three times before the annealing process. After annealing, the furnace tube was pulled out of the furnace and air-cooled to room temperatures before removing the samples for further investigations.

2.3. Characterization

Microstructural investigations in this study were carried out using X-ray diffraction (XRD) and transmission electron microscopy (TEM). The XRD spectra of the synthesized samples were collected using a PANalytical Empyrean Diffractometer with a CuKa (λ = 0.1542 nm) radiation at 45 kV, 40 mA, and 25 °C. Other operating conditions included a scanning range from 20º to 100º, a step size of 0.013º, and a scan rate of 0.044º s^{-1}. The XRD line broadening was used to calculate the average grain size and lattice strain of nanocrystalline Al alloys using the integral breadth analysis and the Averbach formula [28]:

$$\frac{(\beta)2}{tan2\theta o} = \frac{\lambda}{d}\left(\frac{\beta}{tan\theta osin\theta o}\right) + 25 \quad e2 \tag{1}$$

Where β is the measured integral breadth; the full width half maximum (FWHM) of the peak, θo is the diffraction angle, λ is the x-ray wavelength for Cu Kα of 0.154 nm, d is the average grain size, and e is the lattice strain. TEM investigations were carried out using a Thermo Scientific TalosF200X TEM operating at 200 keV to obtain selected area electron diffraction (SAED), bright-field (BF), dark-field

(DF), and STEM-HAADF images. To prepare the samples for TEM analysis, selected particles from the as-milled and as-annealed powder samples were thinned down to a TEM lamella using the (SEM/FIB Versa 3D dual beam, FEI) into a thickness between 25 nm and 75 nm. An in-situ TEM heating experiment was performed on the Al-Li-Sr-GNPs sample to investigate the formation of the second phases. The heating was performed using the Gatan Model 652 Heating Holder. The sample was heated from room temperature up to 673 K at a heating rate of 10°/min. For hardness measurements, both as-milled and annealed powders from each sample were green pressed using uniaxial cold pressing at 1.0 GPa in a tungsten carbide die into disks of 3.0 mm and 1.0 mm diameter and thickness, respectively. Hardness measurements were conducted on the green pressed samples using a Future-Tech Microhardness Tester FM-800 operating at a 25 g load and a 10 s dwell time. A total of 8 measurements were performed on each sample.

3. Results

3.1. Microstructure of the as-milled samples

The XRD patterns of the as milled Al-Li, Al-Li-GNPs, Al-Li-Sr, and Al-Li-Sr-GNPs samples are presented in Fig. 1. The x-ray diffraction patterns indicate the presence of an FCC Al phase in all the as-milled samples. Due to the relatively high solubility limit of Li in Al [35], no Li-related peaks were detected in the XRD patterns, confirming the dissolution of Li in Al lattice and forming the observed FCC solid solution. The absence of any graphitic peaks in the samples with GNPs could be related to the low content of GNPs beyond the XRD detection limit [19,29].

According to the Al/Sr phase diagram [30], Sr is immiscible in Al. Nonetheless, no Sr or Sr-based second phases were observed in the as-milled Al-Li- Sr or the Al-LiSr-GNPs samples, see Fig. 1. This is attributed to the formation of a metastable supersaturated solid solution of Sr in Al after milling. It is well known that ball-milling is a non-equilibrium synthesis technique that could increase the solid solubility of alloying elements beyond the equilibrium limit and even synthesize alloys from immiscible elements, which otherwise do not attain an equilibrium room temperature solubility [3,23]. This is achieved by introducing excess segregation sites in the Al lattice that could enhance diffusivity by ball-milling as a result of the introduced volume fraction of grain boundary and high dislocation densities in nanocrystalline materials [1,31]. Increased solid
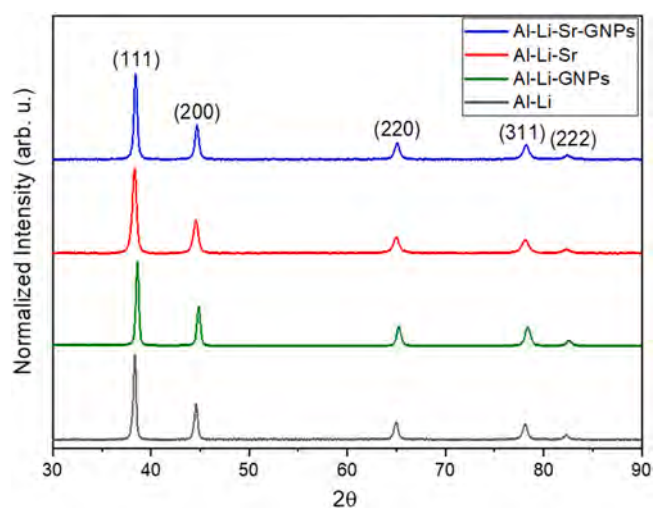

Fig. 1. XRD patterns for the as-milled Al-Li, Al-Li-GNPs, Al-Li-Sr, and Al-Li-Sr-GNPs samples.

solubility limit by ball-milling has been reported for several systems, including Al-Mg [3], Nb-Al [32], Cu-Nb [33], Al-W [34].

Peak broadening was also observed in the XRD patterns for all samples after milling, see Fig. 1. The Averbach formula [28] was used to calculate the grain size and lattice strain from the XRD line broadening, and the results are summarized in Table 1. Nanometric grain size values of 29 nm, 37 nm, 21 nm, and 30 nm were calculated for the as-milled Al-Li, Al-Li-GNPs, Al-Li-Sr, and Al-Li-Sr-GNPs, respectively. The Al-Li and Al-Li-Sr were cryomilled for 4 h only, yet smaller grain sizes were achieved. It has been reported that cryomilling can allow the synthesis of smaller grains at shorter milling times because milling under cryogenic temperatures suppresses the recovery process by eliminating heat buildup, allowing grain refinement to be achieved faster than room temperature milling [35,36]. In addition, the Al-Li-Sr-GNPs achieved a smaller grain size than the Al-Li-GNPs sample even though it was milled at room temperature for the same time. The presence of solute atoms such as Sr in the Al lattice could hinder the dislocation motion during plastic deformation by milling, which could allow more fracturing and achieve a smaller grain size.

The bright-field TEM images and the corresponding SAED patterns of the three as-milled samples can be seen in Fig. 2a–f. The grains in all samples appear to be equiaxed with a random distribution. The ring nature of the corresponding SAED patterns for the three samples confirms the XRD observations of a nanometric structure and verifies the presence of an FCC Al phase as indexed in Fig. 2f. Since the TEM images allow for direct visualization of the grains, it is common practice to confirm the integrity of the XRD calculations by TEM grain size measurements. The ImageJ software was used to measure the grain sizes from different dark-field TEM images. The average grain size values were then calculated based on the analysis of 200 grains from each sample to be 45 ± 6 nm, 15 ± 4 nm, and 29 ± 6 nm for the as-milled Al-Li-GNPs, Al-Li-Sr, and Al-Li-Sr-GNPs samples, respectively. These values fit closely to those average grain size values calculated using the Averbach formula and the XRD patterns. The good agreement between the XRD calculations and the TEM measurements implies the reliability of the XRD method as a grain size calculating tool.

3.2. Microstructure of the annealed samples

To investigate the combined effect of both Sr and GNPs on the thermal stability of the Al-Li nanocrystalline matrix, the Al-Li-GNP, Al-Li-Sr, Al-Li-Sr-GNP as well as the cryomilled Al-Li sample were isothermally annealed at 773 K for 1 h. The XRD patterns for the Al-Li-GNPs, Al-Li-Sr, and Al-Li-Sr-GNPs samples after annealing are shown in Fig. 3a. The broadening of the XRD patterns decreased after annealing at 773 K, signifying a relative increase in grain size and a reduction in lattice strain. The XRD line broadening and the Averbach formula [28] were used to calculate the grain size and lattice strain, and the results are summarized in Table 1. For comparison, the grain size variation of the as milled and annealed samples are plotted in Fig. 3b. The average grain sizes after annealing at 773 K for 1 h for the Al-Li- GNPs, Al-Li-Sr, and Al-Li-Sr-GNPs samples were calculated to be 73 nm, 57 nm, and 70 nm, respectively. Despite the slight increase in grain size, all samples maintained a nanometric grain size.

To further confirm the effect of both Sr and GNPs on the thermal stability of the Sr and/or GNPs containing samples as compared to the unstabilized nanocrystalline Al-Li alloy, TEM was performed on the cryomilled Al-Li sample annealed at 773 K for 1 h, see Fig. 3c. As can be clearly depicted from the bright-field TEM image in Fig. 3c, the annealed Al-Li sample consisted of significantly larger grains (0.5–1.0 μm). The thermal instability of nanocrystalline Al and its alloys at higher temperatures is expected and in agreement with other studies reported in the literature [37,38].

Table 1

Grain size, lattice strain, and hardness of the as-milled and annealed samples.

	Grain Size (nm)		Lattice Strain (%)		Hardness (GPa)	
	298 K	773 K	298 K	773 K	298 K	773 K
Al-2.0 at% Li	29 ± 3	> 500	0.13	–	1.33 ± 0.01	0.53 ± 0.01
Al-2.0 at% Li-1.0 wt% GNPs	37 ± 2	73.0 ± 5	0.16	0.063	1.52 ± 0.03	1.13 ± 0.04
Al-2.0 at% Li-1.0 at% Sr	21 ± 2	57.0 ± 3	0.17	0.09	2.25 ± 0.06	1.36 ± 0.06
Al-2.0 at% Li-1.0 at% Sr-1.0 wt% GNPs	30 ± 3	70.0 ± 3	0.2	0.05	2.1 ± 0.06	1.10 ± 0.05

New lower intensity peaks appeared in the XRD patterns of the annealed Al-Li-Sr and Al-Li-Sr-GNPs samples, see Fig. 3a. According to the Al/Sr phase diagram [30], the main intermetallic compound that can form between Al and Sr is Al_4Sr. Compared to other Al/Sr intermetallics, the formation of Al_4Sr requires lower energy and possesses higher reactivity [39]. The PDF# 00-007-0375 confirmed the identity of the intermetallic, which has a tetragonal crystal structure. The new peaks, which appeared at a Bragg's angle of 31.4°, 32.7°, and 40.4°, are diffracted from the (103), (112), and (200) Al_4Sr atomic planes, respectively. No carbide phases were visible in the XRD patterns at 773 K for GNPs containing samples (Al-Li-GNPs and Al-Li-Sr-GNPs), see Fig. 3a. However, the absence of any carbide XRD peaks does not rule out the formation of the Al_4C_3 phase and could be attributed to its lower content beyond the XRD detection limit. Li et al. [15] reported Al_4C_3 free XRD patterns for their Al-0.25 wt% graphene nanocomposite synthesized by ball-milling and hot-pressing. Nonetheless, the distinct rod-like Al_4C_3 phase was detected following TEM and SAED investigations. The phase diagram of the Al-C system [40] suggests that the Al_4C_3 reaction can occur at a temperature of 823 K. However, experimental investigations on the synthesis of Al/graphene nanocomposites proved the formation of Al_4C_3 phases at lower temperatures. This was accredited to the structural integrity state of the graphene sheets and whether structural defects can serve as initiation sites for the interfacial reaction between Al and C even at temperatures far below the Al melting point [14,40,41]. It is important to note that the intensity of the XRD peaks of each phase is also a representation of the amount of that phase and cannot be related to which second phase forms first, but rather which one is present in a relatively large amount enough to be detected by the XRD. The prepared samples in our study contained 1.0 wt% GNPs and 1.0 at% Sr (which is equivalent to 3.26 wt%). The amount of Sr is about three times higher than the amount of GNPs added. Thus, the XRD peaks of the Al_4Sr second phase are expected to appear more significantly with higher intensities at the same temperature than those of the Al_4C_3 phase.

To investigate the effect of temperature on the formation of the second phases, the Al-Li-Sr-GNPs sample was annealed at 873 K for 1 h; see the XRD patterns in Fig. 3d. The intensity of the Al_4Sr peaks increased with increasing temperature from 773 K to 873 K. In addition, new XRD peaks appeared at a Bragg's angle of 31.5° and 55.2° after annealing at 873 K. According to the PDF #00–035–0799, these peaks are indexed as the (012) and (0015) atomic planes of rhombohedral Al_4C_3. Thus, the XRD peaks of the Al_4C_3 phase, which were undetected by XRD at 773 K, appeared in the sample annealed at 873 K. This proves that the formation of these second phases is temperature driven.
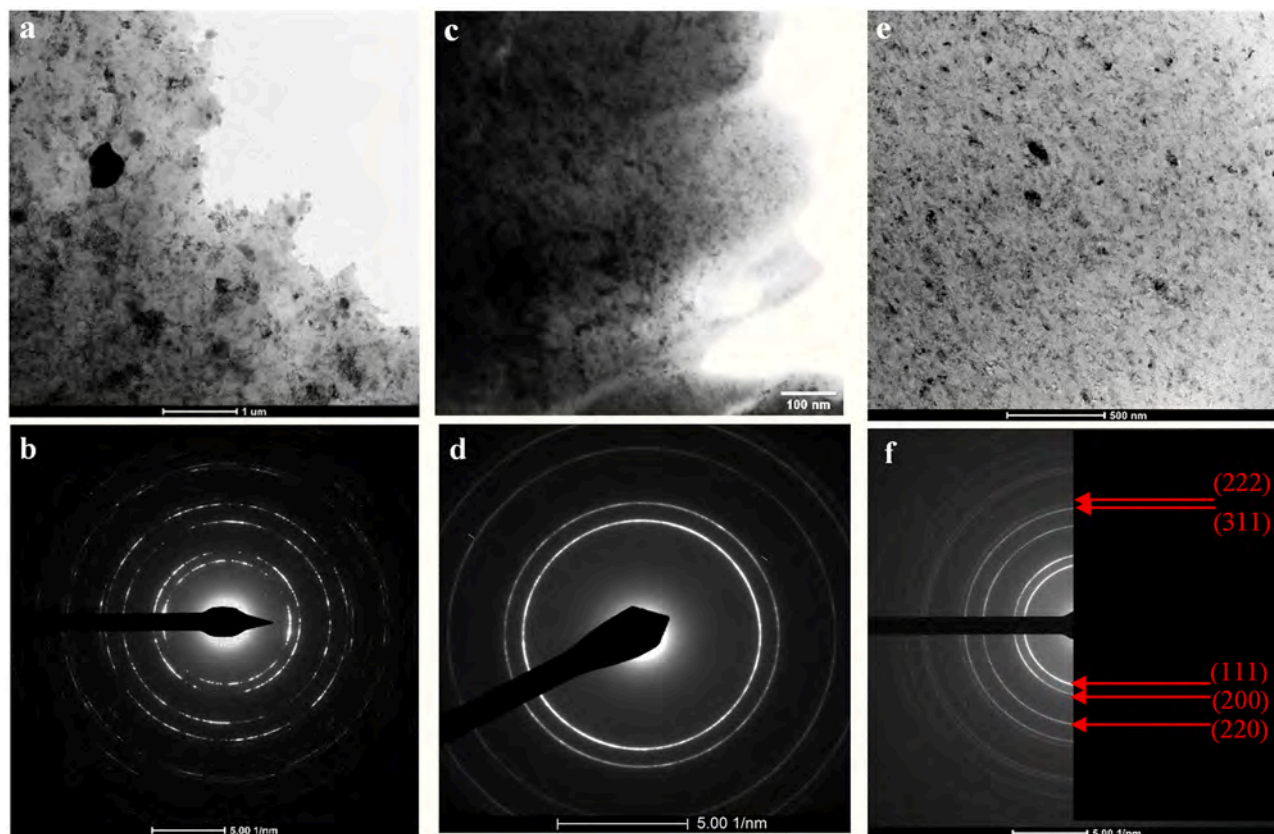

Fig. 2. Bright-field TEM images and the corresponding SAED patterns of the as-milled (a–b) Al-Li-GNPs, (c–d) Al-Li-Sr, and (e–f) Al-Li-Sr-GNPs samples.
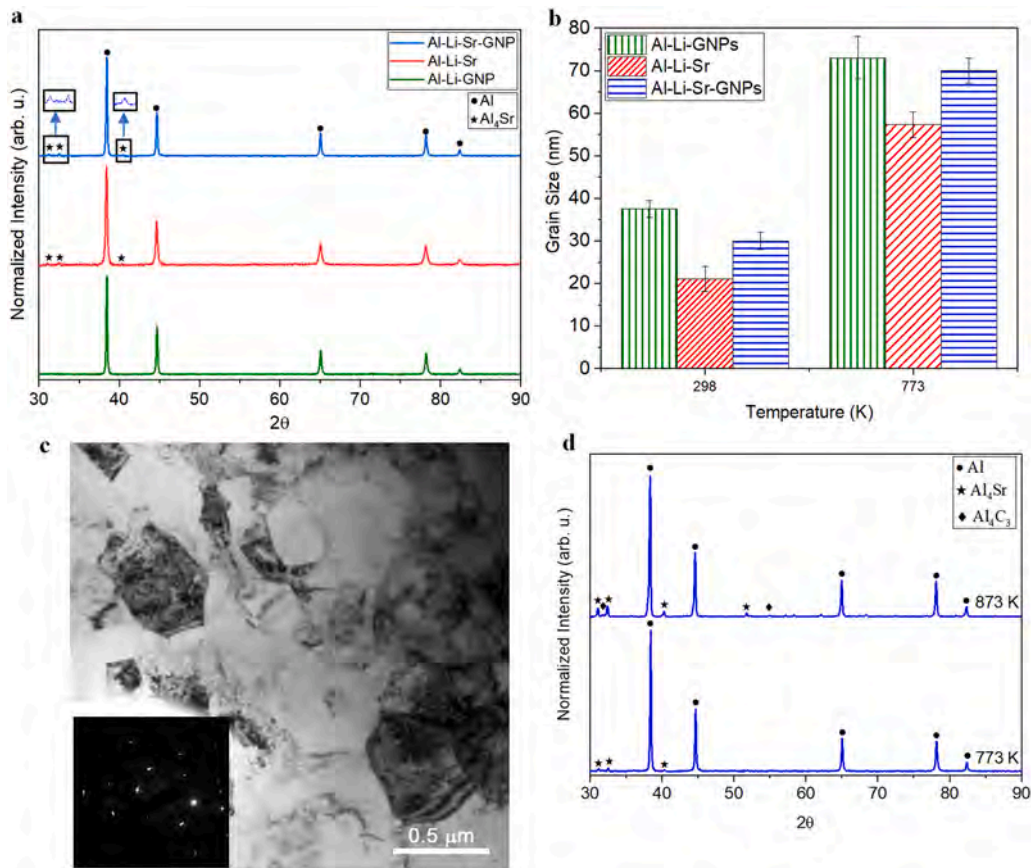
Fig. 3. (a) XRD patterns for the Al-Li-GNPs, Al-Li-Sr, and Al-Li-Sr-GNPs samples annealed at 773 K for 1 h, (b) Calculated average grain sizes for the as-milled and annealed Al-Li-GNPs, Al-Li-Sr, and Al-Li-Sr-GNPs samples, (c) Bright-field TEM image of the Al-Li sample annealed at 773 K for 1 h. Inset image shows the corresponding SAED, and (d) XRD patterns of the Al-Li-Sr-GNPs annealed at 773 K and 873 K for 1 h.

To further investigate the annealed microstructures, TEM analysis was conducted on the Al-Li-GNPs and Al-Li-Sr-GNPs samples annealed at 773 K, see Fig. 4. The presence of the Al_4C_3 and Al_4Sr intermetallic compounds in the samples can be deduced from the presence of the extra indexed rings in the SAED after annealing, see Fig. 4b and d. The presence of the electron diffraction rings of the carbide phase in the SAED patterns at 773 K despite their absence in the XRD pattern for the samples annealed at the same temperature is attributed to the detection limit of the X-ray machine and the higher sensitivity of TEM to detect second phases at lower concentrations. This suggests that the Al_4C_3 phase formed at lower temperatures than suggested by the XRD. Furthermore, the grain size of the Al-Li-Sr-GNPs sample was measured by TEM to confirm the XRD grain size calculations. Based on the analysis of 100 grains, the average grain size of the annealed Al-Li-Sr-GNPs sample was measured to be 82 nm. This value is in close agreement with the 70 nm grain size calculated by XRD, further confirming the reliability of the XRD grain size calculating method.

3.3. Microhardness measurements

Reducing the grain size to the nanoscale must be associated with an enhanced mechanical behavior of the synthesized nano-grained sample. Thus, microhardness measurements can be used as a direct tool for investigating the effect of both Sr and GNPs on the thermal stability of the nanocrystalline Al-Li alloy. Microhardness measurements for the as-milled and annealed Al-Li-GNPs, Al-Li-Sr, and Al-Li-Sr-GNPs samples are plotted in Fig. 5 and are shown in Table 1.

Compared to the starting micro-grained Al with a hardness of 0.42 ± 0.02 GPa, the hardness of the samples dramatically increased

after milling to 1.33 ± 0.01 GPa, 1.52 ± 0.03 GPa, 2.25 ± 0.06 GPa, and 2.1 ± 0.06 GPa, for the Al-Li, Al-Li-GNPs, Al-Li-Sr, and Al-Li-Sr-GNPs samples, respectively. As seen in Fig. 5 and Table 1, a drop in hardness was measured for all samples after annealing at 773 K for 1 h. The thermal instability of the Al-Li sample is yet again confirmed by the significant drop in microhardness from 1.33 ± 0.01 GPa to 0.53 ± 0.01 GPa after annealing. On the contrary, high microhardness values of 1.13 ± 0.04 GPa, 1.36 ± 0.06 GPa, and 1.10 ± 0.05 GPa, were still maintained for the annealed Al-Li-GNPs, Al-Li-Sr, and Al-Li-Sr-GNPs samples, respectively. These values even attained at 773 K are at least 175% higher than the hardness of the starting Al at room temperature.

4. Discussion

The thermal stability of nanocrystalline metals has long been reported in multicomponent systems. The observed thermal stability in nanocrystalline metals was originated from the incorporation of impurities, solutes, second phases, or reinforcements through their interactions with the main nano-grained metal [1,6]. Thus, achieving thermal stability requires the careful design of the system's constituents. In order to analyze the combined effect of GNPs and Sr on the thermal stability of the ball-milled nanocrystalline Al-Li alloy, their separate individual influence on the thermal stability of the Al-Li alloy was first examined.

As mentioned earlier, the cryomilled Al-Li-Sr sample attained a nanometric grain size ~21 nm and a high microhardness of 2.25 GPa after milling. Upon annealing at 773 K, the Al-Li-Sr sample maintained the highest microhardness (1.36 GPa) and also the smallest grain size (57 nm) amongst the rest of the annealed samples. These
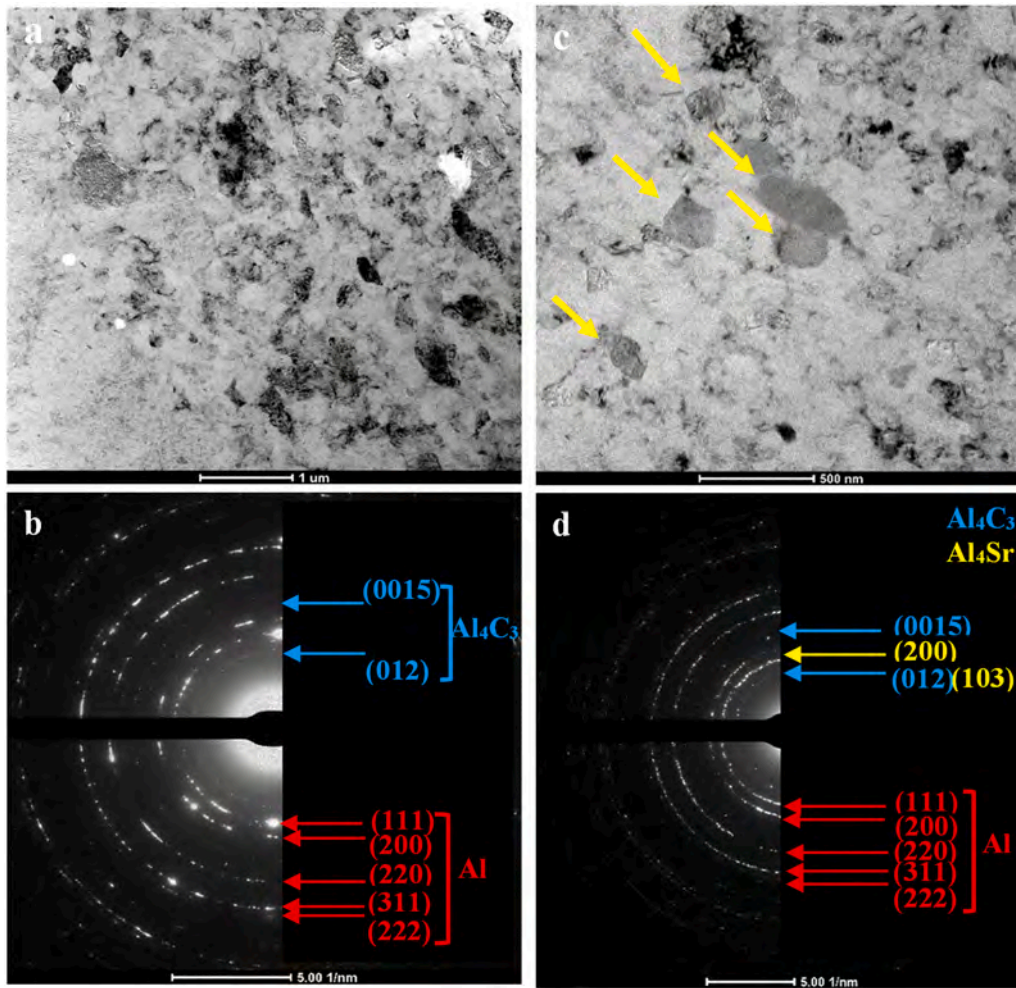
Fig. 4. TEM images and their corresponding SAED patterns of the (a–b) Al-Li-GNPs, and (c–d) Al-Li-Sr-GNPs samples annealed at 773 K for 1 h.
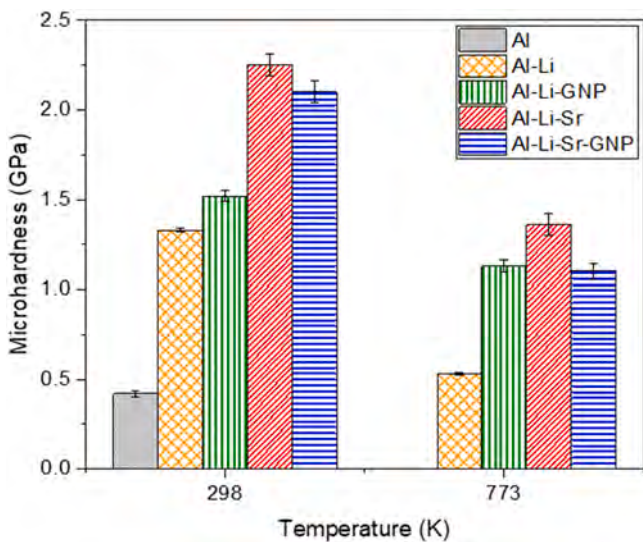

Fig. 5. Hardness vs. temperature for starting Al, Al-Li-Sr, Al-Li-GNPs, and Al-Li-Sr-GNPs samples.

results are in agreement with previous work reporting the effect of Sr on the thermal stability of cryomilled Al [11]. It was indicated by the XRD and SAED patterns in Figs. 1 and 2 that the Sr atoms dissolved in the Al lattice forming a supersaturated solid solution.

Therefore, at low annealing temperatures, the Sr atoms could act as a solute providing both solid-solution strengthening and a solute drag force pinning the grain boundary motion [7]. At intermediate annealing temperatures, the large Sr atoms gained enough thermal energy to diffuse into larger segregation sites at the grain boundaries relieving the extra elastic strain associated with the large atomic misfit from being in the Al lattice. When the broken atomic periodicity of the grain boundaries is reduced by the segregation of solutes, the grain boundary energy reduces, and thermodynamic stability is achieved [6,42]. At this stage, the Sr atoms provide thermodynamic stability by grain boundary segregation [6]. At high enough temperatures, the high thermal energy and low solid solubility between Al and Sr force the Al_4Sr intermetallic phase to form. This is in agreement with the XRD and TEM observations of the Al-Li-Sr sample in Figs. 3d and 4, where the new Al_4Sr peaks started to emerge at 773 K. The effect of Sr on the thermal stability of Al is also confirmed by the TEM images of the Al-Li-Sr sample annealed at 773 K, see Fig. 6a–c. Several round small particles are seen distributed around the grain boundaries of Al in the annealed sample. A magnification of one of the relatively larger particles from Fig. 6a is shown in Fig. 6b to have a diameter of ~27 nm. The corresponding elemental line mapping shown in Fig. 6c confirmed the identity of these particles as the Al_4Sr intermetallic phase.

Similarly, TEM images of the Al-Li-GNPs sample annealed at 773 K can be seen in Fig. 7. Both TEM images in Fig. 7a–c and the elemental mappings in Fig. 7d–e confirm the presence of the distinct rod-like Al_4C_3 second phase. As described earlier, the Al-Li-GNPs
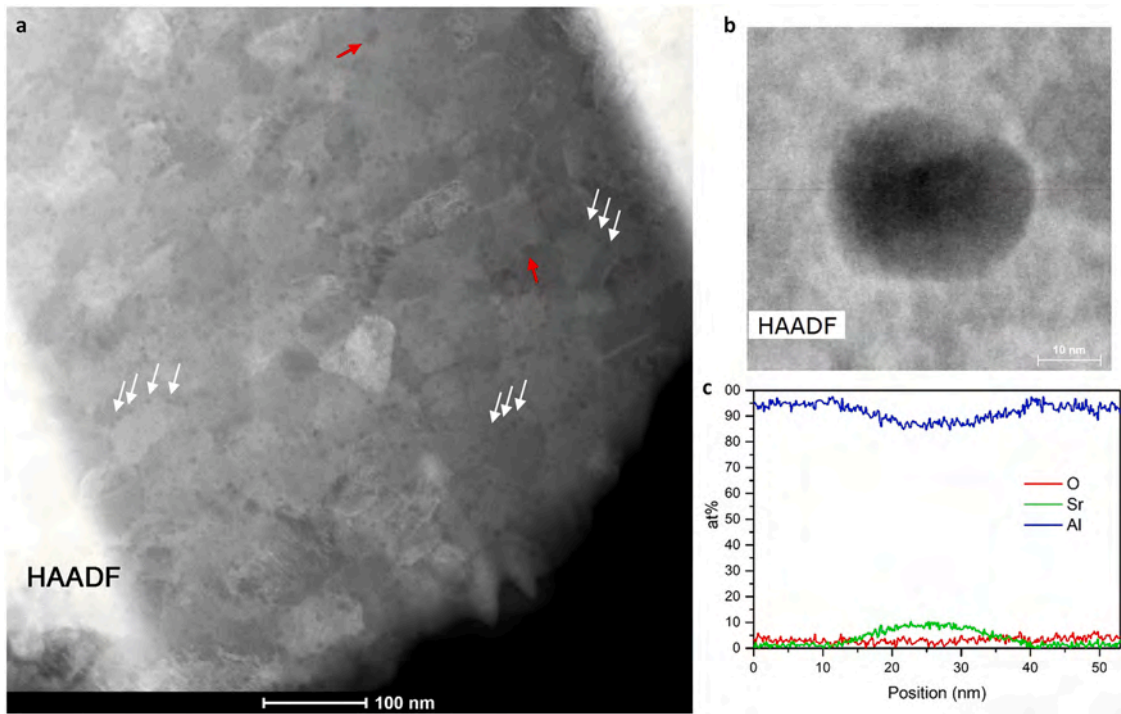
Fig. 6. (a) STEM HAADF image showing the morphology and the distribution of the Al$_4$Sr second phase in the Al-Li-Sr sample annealed at 773 K for 1 h (see white arrows). (b) and (c) A magnification of one of the large Al$_4$Sr particles such as the ones marked by a red arrow in (a) and its corresponding elemental line mapping, respectively.

sample exhibited high thermal stability after annealing at 773 K by maintaining a nanometric grain size and high hardness of 73 nm and 1.13 GPa, respectively, compared to the initial size of 37 nm and

microhardness of 1.5 GPa. Initially, the GNPs acted as a second phase within the Al grains and ensured kinetic stabilization by hindering the grain boundary motion during grain growth. At high
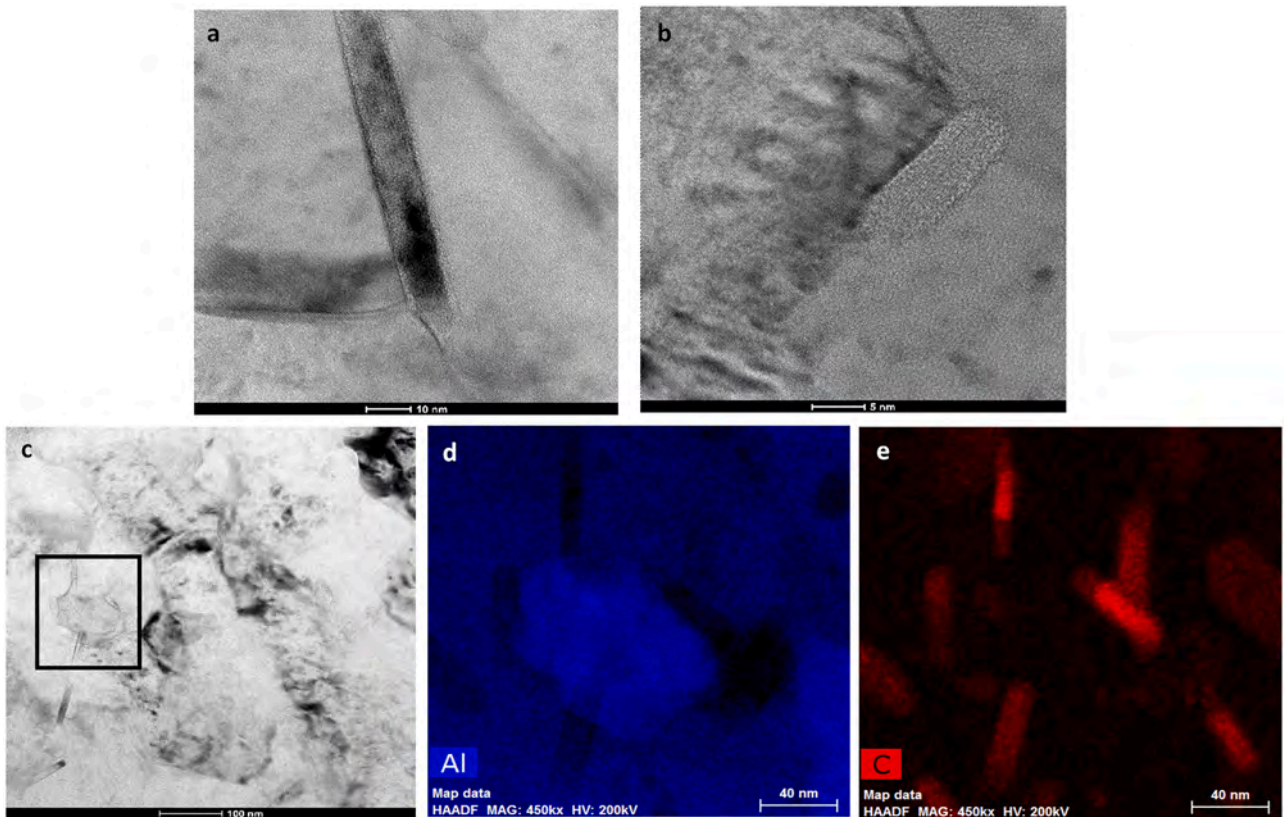

Fig. 7. (a),(b), and (c) TEM image showing the rod-like carbide phase distributed at the grain boundaries in the Al-Li-GNPs sample annealed at 773 K. (d) and (e) Elemental mapping of box area in (c).
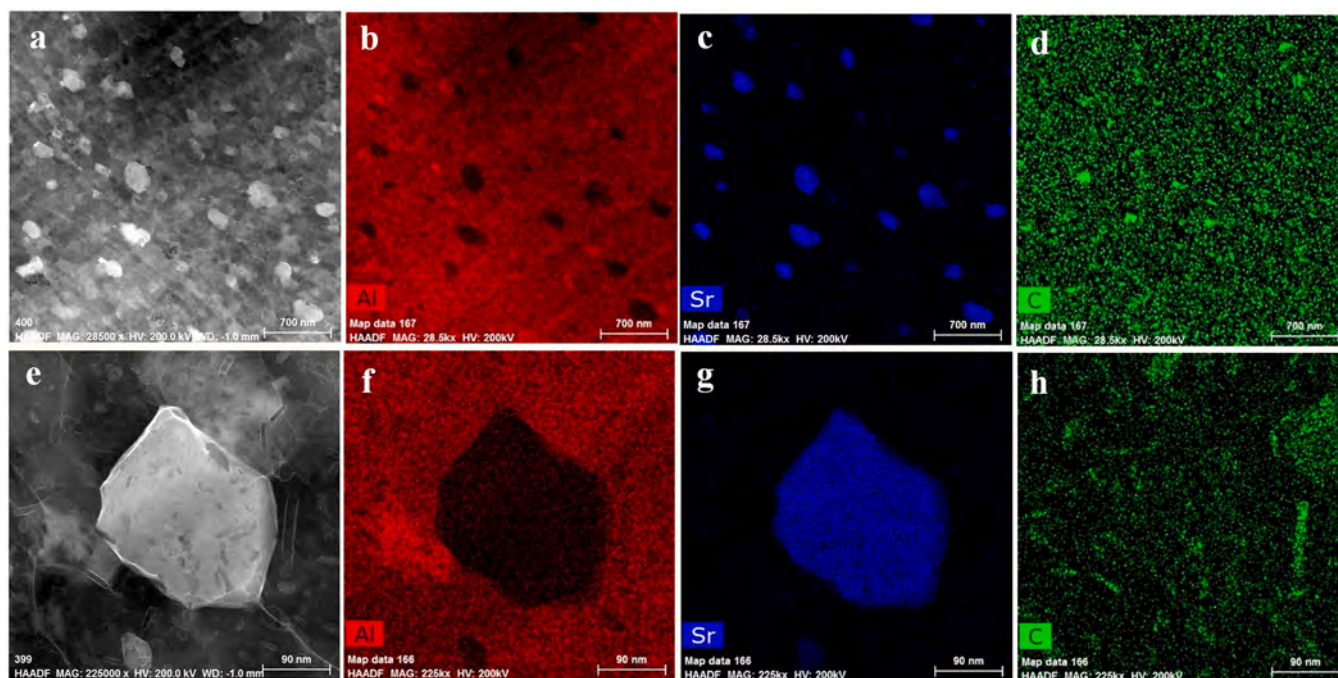
Fig. 8. (a) and (e) STEM HAADF images taken from the Al-Li-Sr-GNPs sample annealed at 773 K for 1 h. (b–d) elemental mapping of (a). (f–h) elemental mapping of (e).

temperatures, the Al_4C_3 phase plays a similar role to that of the Al_4Sr. The reaction between Al and C to form the Al_4C_3 intermetallic phase is a spontaneous reaction that occurs at the Al/graphene interface [21,43]. The rod-like Al_4C_3 phase that is located inside the grains provides kinetic stability. The pinning effect exerted on the grain boundaries of Al by both the GNPs and Al_4C_3 has been observed and briefly discussed [20,43–46]. Studies on the milling of Al and GNPs have extensively reported that the majority of graphene sheets end up distributed at the grain boundaries of Al [18,41,47]. In this case, the carbide phase would also exist at the grain boundaries of Al where it occupies the excess free volume [21,43]. This is confirmed by the TEM images in Fig. 7, which clearly show the rod-like carbide phase distributed at grain boundaries. As a result of this reaction, the broken atomic periodicity of the Al at the grain boundaries is reduced, and a reduction in the grain boundary energy and thus the driving force for grain growth is achieved.

Considering that both the Al_4C_3 and Al_4Sr second phases were proven to exist in the microstructure of the annealed Al-Li-Sr-GNPs sample, see Fig. 3d and the SAED patterns in Fig. 4, this sample would be expected to exhibit the best thermal stability behavior, which would include the least drop in hardness and the smallest grain growth. Nonetheless, the Al-Li-Sr achieved the highest hardness and smallest grain size of 1.36 GPa and 57 nm, respectively, after annealing at 773 K for 1 h. In addition, the Al-Li-GNPs sample exhibited the least grain growth and the lowest hardness drop amongst the three samples. These results indicate the positive effect of adding dilute amounts of both Sr and GNPs as individual elements on the thermal stability behavior of nanocrystalline Al and should therefore contribute to an optimum thermal stability behavior when combined. Nonetheless, grain size calculations and microhardness measurements showed that the Al-Li-Sr-GNPs sample suffered the largest grain growth and attained the lowest hardness upon annealing. In addition, the presence of large irregular grains was observed in the bright-field TEM image of the annealed Al-Li-Sr-GNPs sample, see yellow arrows in Fig. 4c. To investigate the nature of these grains and for a better understanding of this thermal stability behavior, further TEM analysis was conducted. Fig. 8 shows the

STEM HAADF and EDS elemental mapping images taken for the Al-Li-Sr-GNPs sample annealed at 773 K.

The rod-like Al_4C_3 phase can be seen distributed throughout the sample in the STEM HAADF image in Fig. 8e and the corresponding C elemental mapping in Fig. 8 h. Furthermore, the elemental mapping in Fig. 8 indicates that the irregularly large grains correspond to the Al_4Sr phase and is seen located throughout the sample in between the Al grains. Normally, second and intermetallic phases formed as a result of solute segregation at high temperatures in nanocrystalline materials are of small dimensions and are well distributed around the grain boundaries of the host material [48,49]. This is in agreement with the morphology of the Al_4Sr phase observed in Fig. 6 in the Al-Li-Sr sample annealed at 773 K. Instead, irregularly large Al_4Sr particles with an average grain size larger than 250 nm are seen distributed throughout the sample. This unique behavior could be directly correlated to the presence of another second phase, the rod-like Al_4C_3 phase. If both Al_4C_3 and Al_4Sr phases are thermodynamically driven to exist at the grain boundaries, a competition between the two phases will take place. To further understand the competition between the carbide and the intermetallic phase, it is important to understand why the Al_4Sr second phase was not distributed more homogenously at the grain boundaries as in the Al-Li-Sr sample.

As mentioned earlier, it is widely reported that the graphene sheets end up mostly distributed at the grain boundaries of Al after milling, resulting in the carbide phase being mostly distributed at the grain boundaries of Al after annealing as well; see Fig. 7. Therefore, the Al_4Sr agglomeration could be because the grain boundary regions are occupied mainly by the carbide phase after annealing, forcing the Sr to segregate into limited areas and causing the formation of coarse Al_4Sr grains. In addition, it was pointed out earlier that the absence of the Al_4C_3 XRD peaks at lower annealing temperatures can be directly related to its lower concentration than that of the Al_4Sr phase. To investigate whether the Al_4C_3 phase was formed at earlier annealing stages before the formation of the Al_4Sr phase, we conducted an in-situ TEM annealing experiment on the Al-Li-Sr-GNPs sample, see Fig. 9. The in-situ TEM analysis showed that the rod-like carbide phase started forming immediately after
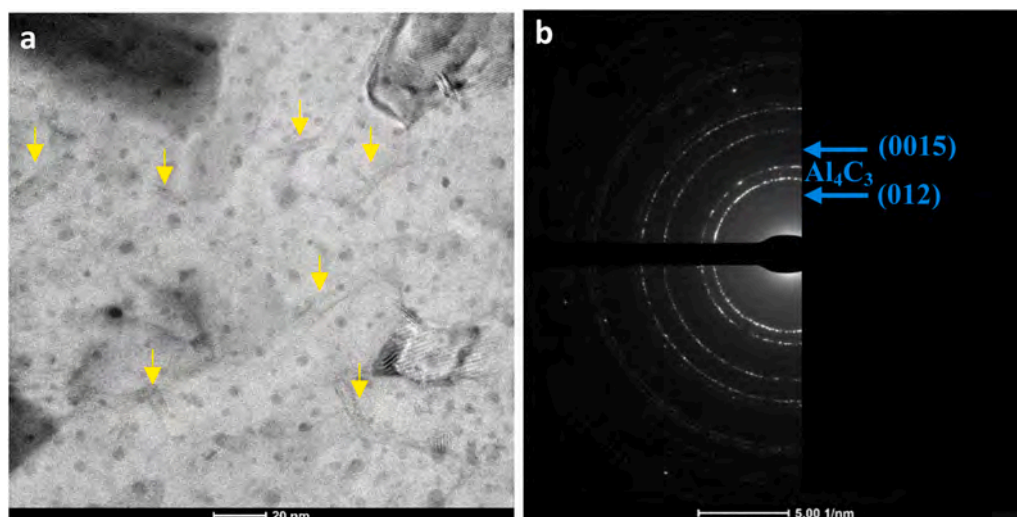
Fig. 9. (a) TEM image of the Al-Li-Sr-GNPs sample taken during an in-situ annealing experiment showing the formation of the rod-like Al_4C_3 phase at 673 K (yellow arrows), and (b) SAED pattern showing the extra Al_4C_3 phase diffraction rings.

the temperature reached 673 K without any holding time at this temperature. This is confirmed by the bright-field TEM image shown in Fig. 9a, which clearly indicates the rod-like carbide phase starting to form at the grain boundaries. The subsequent SAED pattern shown in Fig. 9b shows second phase diffraction rings identified and indexed as the Al_4C_3 phase. Therefore, the early and easy formation of carbides at the grain boundaries at low annealing temperatures before any indication for the formation of the Al_4Sr second phase hindered the proper diffusion of the radially large Sr atoms and subsequently the adequate distribution of the fine Al_4Sr phase at the grain boundaries. Therefore, experimental results showed that the formation of both Al_4Sr and Al_4C_3 is thermally controlled and thermodynamically driven to exist at the grain boundaries of Al. Mixing both GNPs and Sr to induce an enhanced thermal stability behavior of nanocrystalline Al was shown to be competitive and less effective than the thermal stability provided to the nanocrystalline Al-Li alloy by either Sr or GNPs individually.

5. Conclusion

In this study, we investigated the effect of combining two elements, Sr and GNPs, to ball-milled nanocrystalline Al-Li alloy to induce an enhanced thermal stability behavior. Isothermal annealing for 1 h at different temperatures was conducted to examine the thermal stability of the as-milled Al-Li-Sr-GNPs sample. For comparison, two other samples of Al-Li containing either Sr or GNPs alone were examined as well. Nano grain sizes and high microhardness values of 45 ± 6 nm and 1.52 ± 0.03 GPa, 15 ± 4 nm and 2.25 ± 0.06 GPa, and 29 ± 6 nm and 2.1 ± 0.06 GPa, were measured for the as-milled Al-Li-GNPs, Al-Li-Sr, and Al-Li-Sr-GNPs samples, respectively, after milling. After annealing at 773 K for 1 h, the second phase of Al_4Sr was detected distributed around the grain boundaries of Al in the Al-Li-Sr sample. Similarly, rod-like Al_4C_3 phase was distributed at the grain boundaries of Al in the annealed Al-Li-GNPs sample. Despite maintaining a nanometric grain size of 70 nm and a high microhardness value of 1.1 GPa, the Al-Li-Sr-GNPs sample suffered the largest grain growth and attained the lowest hardness upon annealing, compared to the other samples which contained either Sr or GNPs alone. Microstructural investigations revealed that upon annealing, both second phases of Al_4Sr and Al_4C_3 formed by the spontaneous reactions of Al with Sr and Al with C, respectively, in the Al-Li-Sr-GNPs sample. Large particles of an average size larger than 250 nm were identified in the annealed Al-

Li-Sr-GNPs sample as the Al_4Sr second phase. In-situ TEM annealing experiment conducted on the Al-Li-GNPs-Sr sample proved that the Al_4C_3 phase formation preceded the Al_4Sr phase as the rod-like carbide phase was identified by its corresponding diffraction rings after the temperature reached only 673 K. The distribution of the Al_4C_3 rod-like phase at the grain boundaries of Al prevented the proper diffusion of Sr, which lead to its agglomeration in certain regions in the grain boundaries, followed by the agglomeration of the intermetallic Al_4Sr phase at higher temperatures. As a result, this inhibited the positive effect the Sr could have added to the thermal stability of the nanocrystalline Al-Li alloy and resulted in a weakened thermal stability efficiency.

CRediT authorship contribution statement

Sara I. Ahmad: Conceptualization, Data curation, Formal analysis, Investigation, Methodology, Validation, Visualization, Writing – original draft. **Hicham Hamoudi:** Resources, Investigation. **Atef Zekri:** Resources, Investigation. **Khaled M. Youssef:** Conceptualization, Investigation, Methodology, Funding acquisition, Project administration, Supervision, Writing – review & editing.

Declaration of Competing Interest

The authors declare that they have no known competing financial interests or personal relationships that could have appeared to influence the work reported in this paper.

Acknowledgement

References

[1] C. Suryanarayana, Nanocrystalline materials, Int. Mater. Rev. 40 (1995) 41.
[2] C. Suryanarayana, Mechanical alloying and milling, Prog. Mater. Sci. 46 (2001) 1.
[3] K.M. Youssef, R.O. Scattergood, K.L. Murty, C.C. Koch, Nanocrystalline Al–Mg alloy with ultrahigh strength and good ductility, Scr. Mater. 54 (2006) 251.

[4] A. Habibi, M. Ketabchi, M. Eskandarzadeh, Nano-grained pure copper with high-strength and high-conductivity produced by equal channel angular rolling process, J. Mater. Process. Technol. 211 (2011) 1085.

[5] E.O. Hall, Variation of hardness of metals with grain size, Nature 173 (1954) 948.

[6] C.C. Koch, R.O. Scattergood, M. Saber, H. Kotan, High temperature stabilization of nanocrystalline grain size: thermodynamic versus kinetic strategies, J. Mater. Res. 28 (2013) 1785.

[7] C.C. Koch, R.O. Scattergood, K.A. Darling, J.E. Semones, Stabilization of nanocrystalline grain sizes by solute additions, J. Mater. Sci. 43 (2008) 7264.

[8] J.A. Haber, W.E. Buhro, Kinetic instability of nanocrystalline aluminum prepared by chemical synthesis; facile room-temperature grain growth, J. Am. Chem. Soc. 120 (1998) 10847.

[9] V.L. Tellkamp, S. Dallek, D. Cheng, E.J. Lavernia, Grain growth behavior of a nanostructured 5083 Al–Mg alloy, J. Mater. Res. 16 (2001) 938.

[10] F. Zhou, J. Lee, E.J. Lavernia, Grain growth kinetics of a mechanically milled nanocrystalline Al, Scr. Mater. 44 (2001) 2013.

[11] S.I. Ahmad, Thermal Stabilization and Mechanical Properties of Nanocrystalline Al And Al-Li Alloys, Qatar University, Doha, 2016.

[12] M. Saber, H. Kotan, C.C. Koch, R.O. Scattergood, A predictive model for thermodynamic stability of grain size in nanocrystalline ternary alloys, J. Appl. Phys. 114 (2013) 103510.

[13] S.I. Ahmad, H. Hamoudi, A. Abdala, Z.K. Ghouri, K.M. Youssef, Graphene-reinforced bulk metal matrix composites: synthesis, microstructure, and properties, Rev. Adv. Mater. Sci. 59 (2020) 67.

[14] W. Yang, Q. Zhao, L. Xin, J. Qiao, J. Zou, P. Shao, Z. Yu, Q. Zhang, G. Wu, Microstructure and mechanical properties of graphene nanoplates reinforced pure Al matrix composites prepared by pressure infiltration method, J. Alloy. Compd. 732 (2018) 748.

[15] G. Li, B. Xiong, Effects of graphene content on microstructures and tensile property of graphene-nanosheets / aluminum composites, J. Alloy. Compd. 697 (2017) 31.

[16] J.L. Li, Y.C. Xiong, X.D. Wang, S.J. Yan, C. Yang, W.W. He, J.Z. Chen, S.Q. Wang, X.Y. Zhang, S.L. Dai, Microstructure and tensile properties of bulk nanostructured aluminum/graphene composites prepared via cryomilling, Mater. Sci. Eng. A 626 (2015) 400.

[17] F.M. El-Makaty, H.K. Ahmed, K.M. Youssef, Review: The effect of different nanofiller materials on the thermoelectric behavior of bismuth telluride, Mater. Des. 209 (2021) 109974.

[18] M. Tabandeh-Khorshid, J.B. Ferguson, B.F. Schultz, C.-S. Kim, K. Cho, P.K. Rohatgi, Strengthening mechanisms of graphene- and Al2O3-reinforced aluminum nanocomposites synthesized by room temperature milling, Mater. Des. 92 (2016) 79.

[19] A. Bhadauria, L.K. Singh, T. Laha, Combined strengthening effect of nanocrystalline matrix and graphene nanoplatelet reinforcement on the mechanical properties of spark plasma sintered aluminum based nanocomposites, Mater. Sci. Eng. A 749 (2019) 14.

[20] K. Zhan, Y. Wu, J. Li, B. Zhao, Y. Yan, L. Wang, Analysis of recrystallization behavior of shot peened graphene reinforced Al composites during isothermal annealing by X-ray diffraction method, J. Alloy. Compd. 765 (2018) 862.

[21] J. Li, X. Zhang, L. Geng, Effect of heat treatment on interfacial bonding and strengthening efficiency of graphene in GNP/Al composites, Compos. Part A Appl. Sci. Manuf. 121 (2019) 487.

[22] S.I. Ahmed, K.A. Mkhoyan, K.M. Youssef, The activation of deformation mechanisms for improved tensile properties in nanocrystalline aluminum, Mater. Sci. Eng. A 777 (2020) 139069.

[23] S.I. Ahmad, L.A. Al-Sulaiti, K.A. Mkhoyan, K.M. Youssef, Artifact-free bulk nanocrystalline Al-Li alloys with multiple deformation mechanisms and improved tensile properties, Materials Today, Communications 25 (2020) 101607.

[24] M. Muzyk, Z. Pakieła, K.J. Kurzydłowski, Generalized stacking fault energies of aluminum alloys–density functional theory calculations, Metals 8 (2018) 823.

[25] I.J. Polmear, Aluminium alloys – a century of age hardening, Mater. Forum 28 (2004) 1.

[26] R. Pérez-Bustamante, D. Bolaños-Morales, J. Bonilla-Martínez, I. Estrada-Guel, R. Martínez-Sánchez, Microstructural and hardness behavior of graphene-nanoplatelets/aluminum composites synthesized by mechanical alloying, J. Alloy. Compd. 615 (2014) S578.

[27] A. El-Ghazaly, G. Anis, H.G. Salem, Effect of graphene addition on the mechanical and tribological behavior of nanostructured AA2124 self-lubricating metal matrix composite, Compos. Part A Appl. Sci. Manuf. 95 (2017) 325.

[28] H.P. Klug , L.E. Alexander, X-Ray Diffraction Procedures: for Polycrystalline and Amorphous Materials, second ed. (1974).

[29] L.K. Singh, A. Bhadauria, T. Laha, Comparing the strengthening efficiency of multiwalled carbon nanotubes and graphene nanoplatelets in aluminum matrix, Powder Technol. 356 (2019) 1059.

[30] B. Closset, H. Dugas, M. Pekguleryuz, J.E. Gruzleski, The aluminum-strontium phase diagram, Metall. Trans. A 17 (1986) 1250.

[31] H.X. Sui, M. Zhu, M. Qi, G.B. Li, D.Z. Yang, The enhancement of solid solubility limits of AlCo intermetallic compound by high-energy ball milling, J. Appl. Phys. 71 (1992) 2945.

[32] Z. Peng, C. Suryanarayana, F.S. Froes, Mechanical alloying of Nb-Al powders, Metall. Mater. Trans. A 27 (1996) 41.

[33] K.M. Youssef, M.A. Abaza, R.O. Scattergood, C.C. Koch, High strength, ductility, and electrical conductivity of in-situ consolidated nanocrystalline Cu-1%Nb, Mater. Sci. Eng. A 711 (2018) 350.

[34] Y. Ouyang, X. Zhong, W. Wu, Extended solid solubility for Al-W binary system by mechanical alloying, Sci. China Ser. A Math. 43 (2000) 180.

[35] S.-H. Back, G.-H. Lee, S. Kang, Effect of cryomilling on particle size and microstrain in a WC-Co alloy, Mater. Trans. 46 (2005) 105.

[36] J. Lee, F. Zhou, K.H. Chung, E.J. Lavernia, N.J. Kim, Grain growth of nanocrystalline Ni powders prepared by cryomilling, Metall. Mater. Trans. A 32 (2001) 3109.

[37] C.L. De Castro, B.S. Mitchell, Crystal growth kinetics of nanocrystalline aluminum prepared by mechanical attrition in nylon media, Mater. Sci. Eng. A 396 (2005) 124.

[38] H.R. Ammar, K.A. Khalil, E.-S.M. Sherif, Thermally stable nanocrystalline aluminum alloys processed by mechanical alloying and high frequency induction heat sintering, Int. J. Mater. Metall. Eng. 9 (2015) 154.

[39] C. Liao, J. Chen, Y. Li, R. Tu, C. Pan, Morphologies of Al4Sr intermetallic phase and its modification property upon A356 alloys, J. Mater. Sci. Technol. 28 (2012) 524.

[40] S.N. Alam, L. Kumar, Mechanical properties of aluminium based metal matrix composites reinforced with graphite nanoplatelets, Mater. Sci. Eng. A Struct. Mater. Prop. Microstruct. Process. 667 (2016) 16.

[41] H. Zhang, C. Xu, W. Xiao, K. Ameyama, C. Ma, Enhanced mechanical properties of Al5083 alloy with graphene nanoplates prepared by ball milling and hot extrusion, Mater. Sci. Eng. A 658 (2016) 8.

[42] H.R. Peng, M.M. Gong, Y.Z. Chen, F. Liu, Thermal stability of nanocrystalline materials: thermodynamics and kinetics, Int. Mater. Rev. 62 (2017) 303.

[43] A. Santos-Beltrán, R. Goytia-Reyes, H. Morales-Rodriguez, V. Gallegos-Orozco, M. Santos-Beltrán, F. Baldenebro-Lopez, R. Martínez-Sánchez, Characterization of Al–Al4C3 nanocomposites produced by mechanical milling, Mater. Charact. 106 (2015) 368.

[44] W. Zhou, Y. Fan, X. Feng, K. Kikuchi, N. Nomura, A. Kawasaki, Creation of individual few-layer graphene incorporated in an aluminum matrix, Compos. Part A Appl. Sci. Manuf. 112 (2018) 168.

[45] Y. Xie, X. Meng, Y. Huang, J. Li, J. Cao, Deformation-driven metallurgy of graphene nanoplatelets reinforced aluminum composite for the balance between strength and ductility, Compos. Part B Eng. 177 (2019) 107413.

[46] B. Xiong, K. Liu, W. Xiong, X. Wu, J. Sun, Strengthening effect induced by interfacial reaction in graphene nanoplatelets reinforced aluminum matrix composites, J. Alloy. Compd. 845 (2020) 156282.

[47] X. Gao, H. Yue, E. Guo, H. Zhang, X. Lin, L. Yao, B. Wang, Preparation and tensile properties of homogeneously dispersed graphene reinforced aluminum matrix composites, Mater. Des. 94 (2016) 54.

[48] S.C. Pun, W. Wang, A. Khalajhedayati, J.D. Schuler, J.R. Trelewicz, T.J. Rupert, Nanocrystalline Al-Mg with extreme strength due to grain boundary doping, Mater. Sci. Eng. A 696 (2017) 400.

[49] P. Biswas, A. Biswas, R. Bhandari, M.K. Mondal, Microstructure, mechanical properties and fracture behavior of in-situ Al-5Mg-Al4Sr composite, Mater. Today Commun. 15 (2018) 190.